# Variability in GRMHD Simulations of Sgr A\*: Implications for EHT Closure Phase Observations

Lia Medeiros <sup>1,2</sup>, Chi-kwan Chan<sup>1</sup>, Feryal Özel<sup>1</sup>, Dimitrios Psaltis<sup>1</sup>, Junhan Kim<sup>1</sup>, Daniel P. Marrone<sup>1</sup>, and Aleksander Sądowski<sup>3</sup>

Steward Observatory and Department of Astronomy, University of Arizona, 933 N. Cherry Avenue, Tucson, AZ 85721, USA

Department of Physics, Broida Hall, University of California Santa Barbara, Santa Barbara, CA 93106, USA

MIT Kavli Institute for Astrophysics and Space Research, 77 Massachusetts Avenue, Cambridge, MA 02139, USA

Received 2016 October 10; revised 2017 May 31; accepted 2017 May 31; published 2017 July 19

#### **Abstract**

Closure phases along different baseline triangles carry a large amount of information regarding the structures of the images of black holes in interferometric observations with the Event Horizon Telescope. We use long time span, high cadence, GRMHD+radiative transfer models of Sgr  $A^*$  to investigate the expected variability of closure phases in such observations. We find that, in general, closure phases along small baseline triangles show little variability, except in the cases when one of the triangle vertices crosses one of the small regions of low visibility amplitude. The closure phase variability increases with the size of the baseline triangle, as larger baselines probe the small-scale structures of the images, which are highly variable. On average, the funnel-dominated MAD models show less closure phase variability than the disk-dominated SANE models, even in the large baseline triangles, because the images from the latter are more sensitive to the turbulence in the accretion flow. Our results suggest that image reconstruction techniques need to explicitly take into account the closure phase variability, especially if the quality and quantity of data allow for a detailed characterization of the nature of variability. This also implies that, if image reconstruction techniques that rely on the assumption of a static image are utilized, regions of the u-v space that show a high level of variability will need to be identified and excised.

Key words: accretion, accretion disks - black hole physics - Galaxy: center - radiative transfer

#### 1. Introduction

The Event Horizon Telescope (EHT), a 1.3 mm wavelength VLBI experiment, will image, for the first time, black holes at event horizon scales (see, e.g., Doeleman et al. 2009a). One of the primary observing targets for the EHT is Sagittarius A\* (Sgr A\*), the supermassive black hole at the center of our galaxy. Sgr A\* is an ideal candidate for the EHT since it has the largest angular size among the known nearby black holes (Johannsen et al. 2012), a well measured mass and distance (Ghez et al. 2008; Gillessen et al. 2009), and has been extensively studied at a variety of wavelengths for over a decade (see Baganoff et al. 2001 and Genzel et al. 2003 for early studies).

The EHT will, in principle, measure visibility amplitudes and phases, which are the complex components of the Fourier transform of the image. However, millimeter wavelength VLBI interferometers cannot measure absolute phases at each u-v point covered by the array. This is because there are no point sources that are both close enough to Sgr A\* and bright enough at 1.3 mm to be used for calibration and because the timescale for variability of the atmospheric interference at 1.3 mm due to water vapor is only of the order of 10 s (Doeleman et al. 2002). Instead, the EHT will measure closure phases, which are the sum of phases at three points in u-v space, such that the effect of the atmosphere at each telescope cancels out (Jennison 1958). The EHT has already obtained closure phase data for Sgr A\* for the Hawaii, Arizona, California (HI–AZ–CA) triangle. Fish et al. (2016) reported a median closure phase of +6°3 over 13 observing nights during a four-year period. The positive, non-zero average closure phase demonstrates that Sgr A\* is not circularly symmetric on event horizon scales.

Even though closure phase measurements eliminate the variability due to atmospheric interference, they do not mitigate the effects of intrinsic source variability. Indeed, the flux from

Sgr A\* has been observed to be variable at many wavelengths, including at 1.3 mm (e.g., Marrone et al. 2008; Porquet et al. 2008; Do et al. 2009). The EHT observed variability at 1.3 mm on scales of a few Schwarzschild radii (Fish et al. 2011). The dynamical timescale, for Sgr A\* at event horizon scales is about 10 minutes. In contrast, the imaging timescale for the EHT is of the order of hours because the interferometer relies on the rotation of the Earth to map out the u–v space. This points to the necessity of taking the intrinsic source variability into account when analyzing EHT data (see, e.g., Lu et al. 2016) but also offers the potential of using source variability to probe the spacetime of the black hole near its horizon (Doeleman et al. 2009a).

A number of groups have considered the effects of closure phase variability in interpreting EHT data. Doeleman et al. (2009b) used a semi-analytic model to explore the variability in closure phases caused by an orbiting hot spot for a few EHT closure triangles. Dexter et al. (2010) performed an early study of the properties of closure phase variability in GRMHD simulations focusing on disk-dominated models and triangles, which are appropriate for the already existing EHT observations. Broderick et al. (2011) compared stationary semi-analytic models with variable normalization to early EHT closure phase data. Broderick et al. (2016) studied closure phases for the HI-AZ-CA triangle in a stationary semi-analytic accretion flow model, when small-scale Gaussian brightness fluctuations were introduced. Fraga-Encinas et al. (2016) used two GRMHD models, one funnel dominated and one disk dominated, to explore the effect of the Earth's rotation on the variability of closure phases in the HI-AZ-CA triangle but did not include the effect of intrinsic source variability.

In this paper, we aim to characterize the expected properties of closure phases for Sgr A\* in a wide range of EHT triangles of various sizes and orientations, using a suite of disk- and

funnel-dominated GRMHD+radiative transfer simulations. We employ five long time span models that probe a range of black hole spins, initial magnetic field geometries, and thermodynamic prescriptions for the electrons (see Chan et al. 2015a, 2015b for details of the models). The parameters of the models, which we review in Section 2, have been calibrated to fit the broadband spectra, the 1.3 mm image size, and were then shown to be consistent with the multi wavelength variability of Sgr A\* (see Ball et al. 2016). In Section 3, we investigate the expected magnitudes of the interferometric visibility phases throughout the u-v plane. Even though the EHT will not be able to directly measure the visibility phases at individual locations on the u-v plane, exploring their properties allows us to understand in Section 4 the variability of the closure phases that the EHT will measure. We conclude in Section 5 and compare our results to the existing limited number of closure phase measurements from Sgr A\* on a single baseline triangle (Fish et al. 2016).

#### 2. The GRMHD+Ray Tracing Simulations

In previous work, we considered a large number of GRMHD + radiative transfer simulations where we varied the black hole spin, the initial geometry of the magnetic field, the accretion rate, and the thermodynamic prescription for the electrons (Chan et al. 2015b). We created these models using HARM (Gammie et al. 2003) for the GRMHD simulations (Narayan et al. 2012; Sądowski et al. 2013) and GRay (Chan et al. 2013) to solve the radiative transfer equation along null geodesics. As discussed in Chan et al. (2013), our dynamical simulations were performed under the assumptions of ideal MHD and radiative transfer calculations were performed using the fastlight approximation. We calibrated the simulations using Sgr  $A^*$  data. Specifically, we enforced the following constraints: (a) a flux and a slope in the  $10^{11}$ – $10^{12}$  Hz range that matches observations, (b) a flux at  $\approx 10^{14}$  Hz that falls within the observed range of the highly variable infrared flux, (c) an X-ray flux that is consistent with 10% of the observed quiescent flux, i.e., the percentage that has been attributed to emission from the inner accretion flow (Neilsen et al. 2013), and (d) the size of the emission region that is consistent with the size determined by the early EHT observations (Doeleman et al. 2008).

We use a threshold in plasma  $\beta$  to define two regions: the disk ( $\beta > 0.2$ ) and the funnel, which is a low density region dominated by magnetic pressure ( $\beta < 0.2$ ). We use a constant electron-to-ion temperature ratio for the disk region and consider two possible, physically motivated models for the funnel region. In the first model, we assume a constant electron-to-ion temperature ratio (which is different than the ratio for the disk region) and, in the second, a constant electron temperature. These models reproduce a disk/funnel structure that is similar to the results discussed in Ressler et al. (2017), who use a more detailed treatment developed to model particle heating in the solar wind (Howes 2010, 2011).

From our large suite of simulations, we identified five models that fit all observational constraints. All models have an observer inclination of  $i=60^{\circ}$  with respect to the spin axis of the black hole. Model A has a black hole spin of a=0.7, an initial magnetic field geometry that leads to weak, turbulent fields near the horizon (Standard and Normal Evolution; SANE), and a plasma model with a constant electron temperature for the funnel region. Model B is the same as Model A but with a black hole spin of a=0.9.

Table 1
Summary of our Five Models

Name	а	$B_0$	$n_{\mathrm{e}}$	$\theta_{ m disk}$	$T_{ m e,funnel}$	$\theta_{\mathrm{funnel}}$
A	0.7	SANE	$6.885 \times 10^{7}$	0.02371	56.23	
В	0.9	SANE	$5.465 \times 10^{7}$	0.01000	31.62	
C	0.0	MAD	$5.932 \times 10^{8}$	0.00056		0.01000
D	0.9	MAD	$1.599 \times 10^{8}$	0.00075	1.78	
E	0.9	MAD	$1.599 \times 10^{8}$	0.00075		0.00316

**Note.** Summary of the five best-fit models from Chan et al. (2015b). The first column lists the model names used throughout the paper. The second and third columns list the black hole spin (a) and the accretion flow state that depends on the initial magnetic field geometry ( $B_0$ ). The fourth column refers to the density normalization ( $n_e$ ) while the fifth column refers to the electron-to-ion temperature ratio in the disk ( $\theta_{\text{disk}}$ ). The last two columns refer to the treatment of the funnel region, we consider two plasma models: one with a constant electron temperature for the funnel ( $T_{e,\text{funnel}}$ ) and the other with a constant electron-to-ion temperature ratio for the funnel ( $\theta_{\text{funnel}}$ ).

Models C-E, in contrast, have an initial magnetic field geometry that leads to coherent magnetic field structures near the horizon (MAD, Magnetically Arrested Disk). In addition, Model C has a black hole spin of a = 0.0 and a plasma model with a constant electron-to-ion temperature ratio for the funnel region. Model D has a black hole spin of a = 0.9 and, again, a plasma model with a constant electron-to-ion temperature ratio for the funnel region. Model E is like Model D but uses a plasma model with a constant electron temperature in the funnel region. For all models, the values for the normalization of the electron number density, the electron-to-ion temperature ratio for the disk and funnel and/or the electron temperature for the funnel were fit to the observations described above (see Chan et al. 2015b for detailed model parameters). We use 1024 snapshots from each simulation with a time resolution of  $10GMc^{-3}$  or  $\approx 3.5$  minutes, which results in a total time span of approximately 60 hr. Table 1 summarizes the parameters of the models we consider.

Figure 1 shows the average 1.3 mm wavelength images for the five simulations we consider. Models A and B, the SANE models, have 1.3 mm wavelength emission regions that are dominated by the thick accretion disk. The emission from these models is asymmetric due to the effects of relativistic Doppler beaming, because the part of the orbiting accretion flow that is coming toward the observer is beamed and appears brighter than the part that is moving away from the observer. The MAD models, (C, D, and E), however, have 1.3 mm wavelength emission regions that are dominated by the funnel regions. Model C is unique in that its emission is dominated by the footpoints of the funnel region with negligible emission coming from the disk. Models D and E have emission coming from both the Doppler beamed disk and the funnels.

The red circles superimposed on the images correspond to the size of the black hole shadow predicted by general relativity. For comparison, the red dots show the location of the center of the black hole. Frame dragging effects cause the emission to be offset (red circles are not centered on the black hole) for models that have a non-zero spin. The red stars in the figures indicate the calculated center of light for each image. The center of light was used in the calculation of the Fourier transform of the image, as we will discuss in Section 3.

Figure 2 shows a few example snapshots from models B and D. We can see that the disk-dominated model (Model B) shows

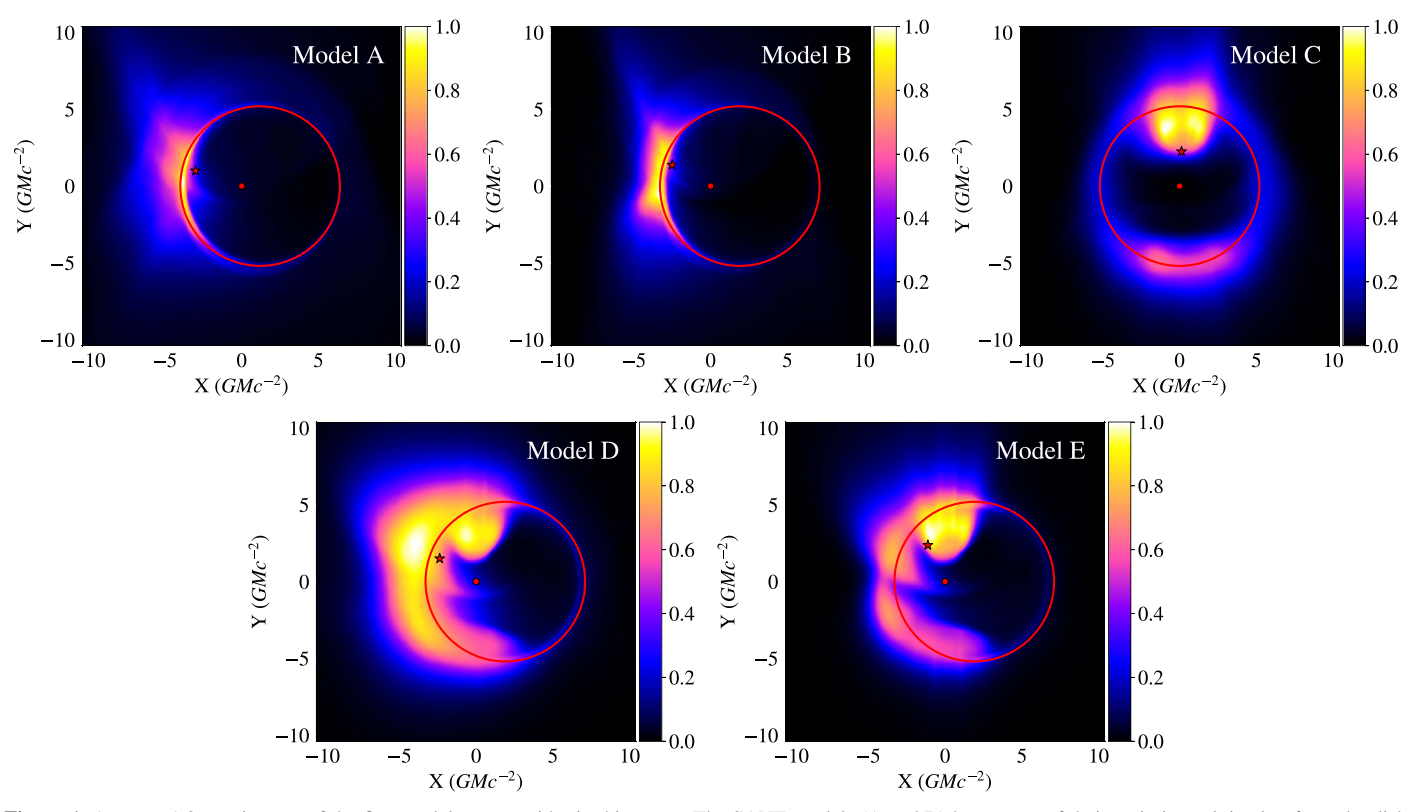


**Figure 1.** Average 1.3 mm images of the five models we consider in this paper. The SANE models (A and B) have most of their emission originating from the disk region, while the MAD models (C, D, and E) have significant emission originating from the footpoints of the funnels. Model C is unique, with negligible emission from the disk and a black hole spin of zero. The red circles indicate the expected size of the black hole shadow according to general relativity. The red stars correspond to the location of the center of light for each model while the red dots are the location of the center of the black hole. Since the orientation of Sgr A\* on the sky is not known, these images show an arbitrary orientation where the spin axis of the black hole points north. The maximum intensity in each panel has been normalized to unity.

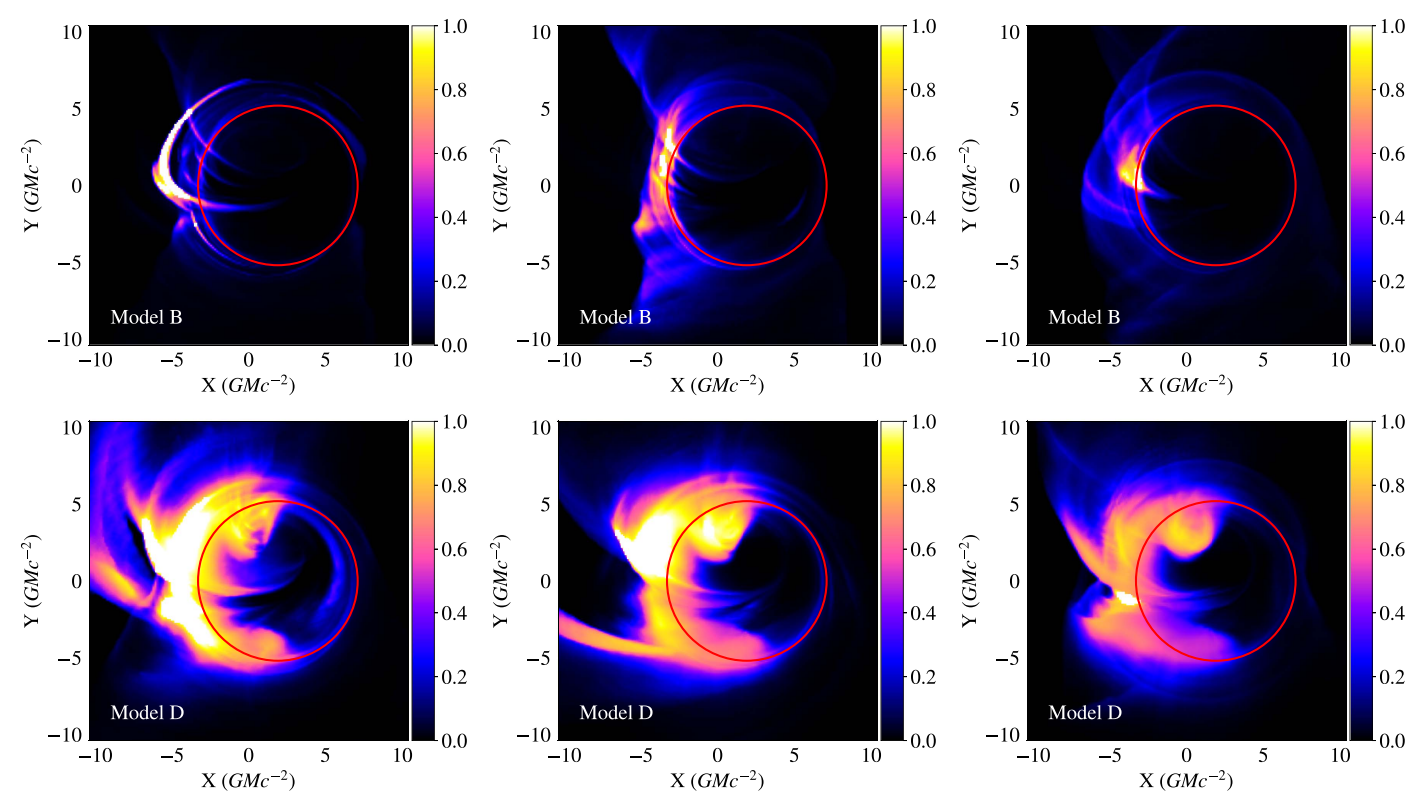


**Figure 2.** Several example snapshots from Model B (top row) and Model D (Bottom row) showing significant structural variation of the image with time. All snapshots have the same brightness normalization such that differences in brightness between snapshots are real. Although SANE models are more variable, MAD models still show significant variability.

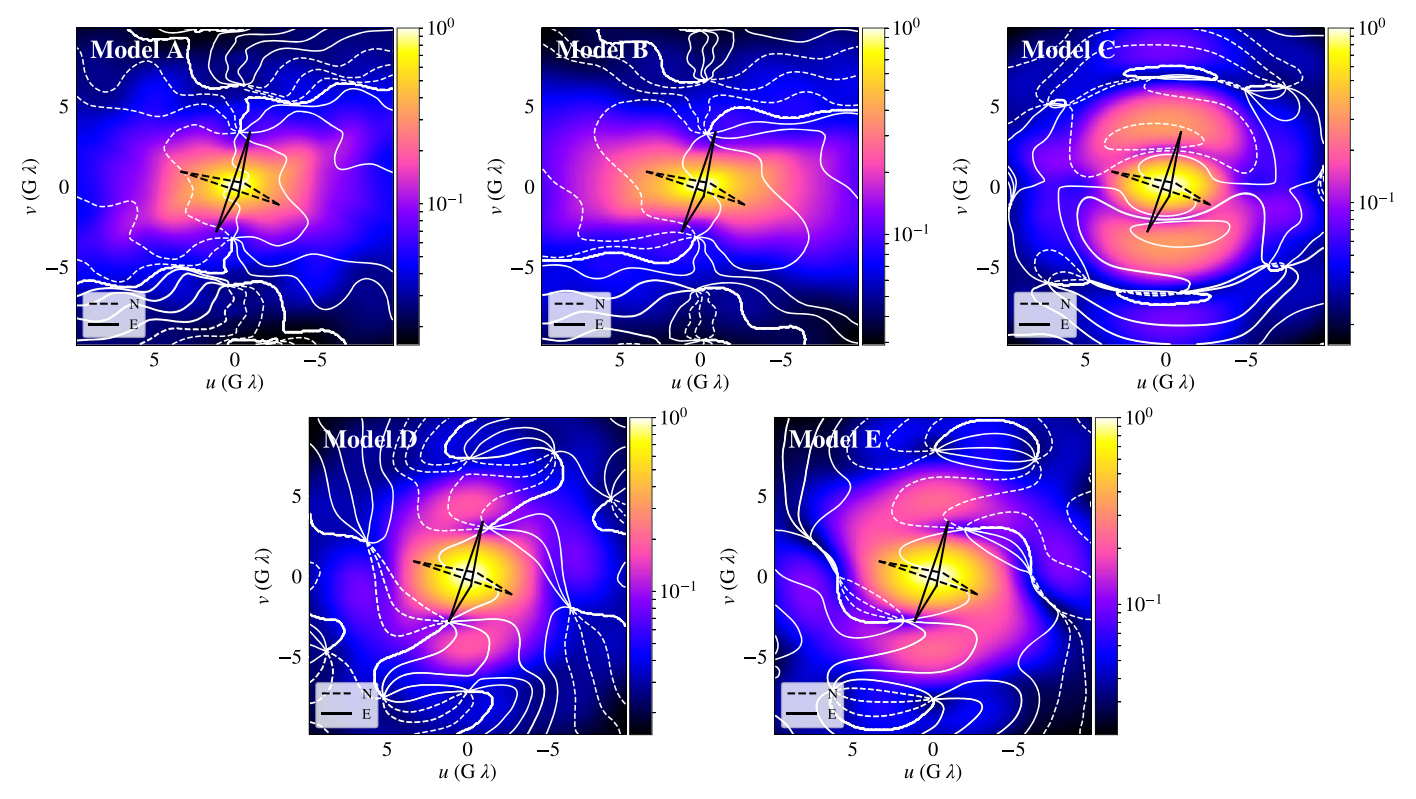


Figure 3. Color maps show the average visibility amplitudes and the white contours show the average visibility phases for the five models. Minima in the visibility amplitudes correspond to steep gradients in visibility phases. The black dashed triangles correspond to the HI–AZ–CA triangle for a black hole with a spin axis pointing north, while the solid black triangles correspond to the same HI–AZ–CA triangle for a black hole with spin axis pointing east. The visibility amplitude maps have been normalized to unity.

significant structural changes in the images with time as opposed to a constant structure with varying flux. In large part, these variations are caused by short lived flux tubes that come in and out of the line of sight. However, there is also significant variability in the thickness and structure of the crescent. The hybrid model (Model D) has a funnel component and a disk component in its emission region. In general, models like this show less overall variability than the disk-dominated models but still show significant structural changes with time.

### 3. Visibility Phases

Since the EHT is an interferometer, it will observe the visibilities, or the complex Fourier components, of the image of Sgr A\*. The amplitudes of these Fourier components, or visibility amplitudes, for our five models have been discussed in Medeiros et al. (2016). Here we focus on the phases of the complex Fourier components, or visibility phases.

Due to the effects of gravitational lensing and Doppler beaming, the emission predicted by these models is not centered on the black hole (the red stars and red dots in Figure 1 are in different locations), which results in an overall rapid gradient in phase. We removed this unmeasurable phase gradient by shifting the snapshots such that the center of light of the images (the red stars in Figure 1) coincide with the center of the average image (red dots in Figure 1) before calculating the transforms. We performed the same shift for all snapshots within each simulation such that they all have the same phase centers.

In Figure 3, we present the structure of the complex visibilities for the different GRMHD models denoting the

average visibility phases with contours and the visibility amplitudes in color maps. These averages are obtained by finding the phases and amplitudes of each snapshot and subsequently averaging them. Because angles are directional, periodic quantities, we need to employ a method for calculating means that is appropriate for them. In the Appendix, we describe the directional statistic we use hereafter.

Figure 3 highlights the fact that minima in visibility amplitudes coincide with steep gradients in phase. This is particularly prominent in the MAD models (C, D, and E), which have clear minima that are preserved in the average of the visibility amplitudes as we showed in our previous paper (Medeiros et al. 2016). In each panel, the black dashed (solid) triangle corresponds to the HI–AZ–CA closure triangle for a black hole with spin axis pointing north (east). For brevity, we plotted the visibility amplitude and phase averages of the black hole at a constant (north) orientation but moved the triangle so that the relative orientation of the visibilities and the triangles is correct for the quoted black hole spin axis orientation. In reality, the orientation of the triangle is fixed and the orientation of the black hole in the sky is unknown. We will discuss these triangles further below.

We explore the structure of the variability in the visibility phases in Figure 4, where the dispersion in visibility phases is shown in color, while the average visibility phases are shown as white contours for comparison. The dispersion was calculated by taking into account the fact that angles are directional quantities, as discussed in the Appendix. The directional dispersion, D (see Equation (4)), is approximately equal to  $\sigma^2/2$  for small  $\sigma$ , where  $\sigma$  is the dispersion of a non-directional Gaussian distribution, and approaches unity in the

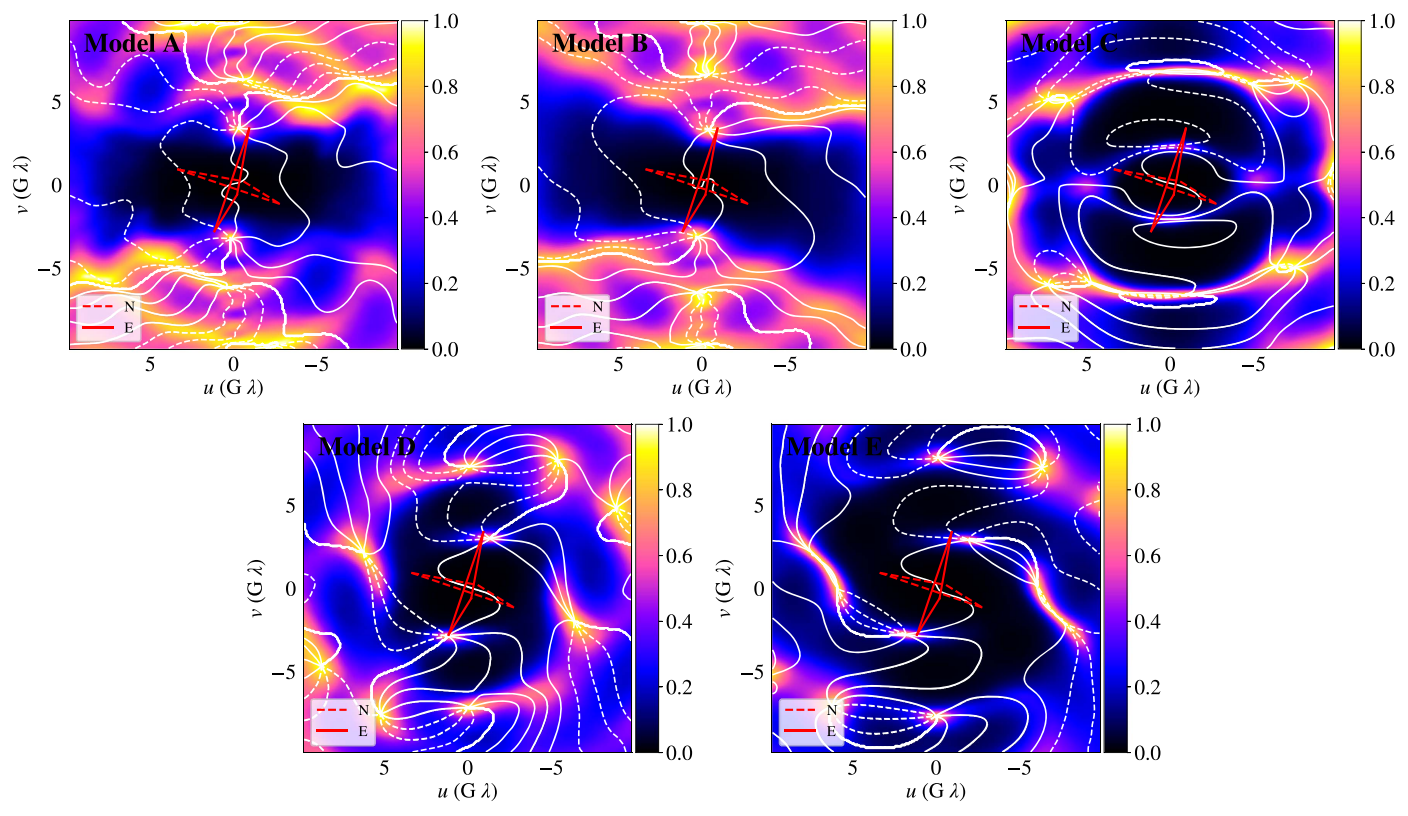


Figure 4. Color map shows the dispersion in visibility phase at each point in the u-v space throughout each  $\sim$ 60 hr simulation. These dispersions were calculated using the directional statistics described in the Appendix. The white contours correspond to the average phase. Regions of steep phase gradients (and minimum amplitudes; see Figure 3) correspond to large dispersion in visibility phase. The red dashed (solid) triangle corresponds to the HI–AZ–CA closure triangle for a black hole with spin axis pointing north (east).

limit of a flat distribution. In the figure, the black and dark blue regions have small dispersions, while the yellow or white regions have very broad, and possibly flat distributions. For reference, D=0.5 shown in pink corresponds to a Gaussian with a standard deviation of about 1 rad or  $57^{\circ}$ .

Figure 4 shows two general characteristics of variability in the visibility phase throughout the u-v plane. First, for each model, there are a number of localized regions on the u-v plane that exhibit very large dispersions in phase. These regions coincide with the locations of the minima in the visibility amplitudes. Phase variability is related to visibility amplitude since, for similar perturbations in its real and imaginary components, a vector with larger magnitude will experience a smaller change in phase. This means that, if all complex Fourier components of the image experience perturbations to their real and imaginary components of similar size, the complex vectors with smaller amplitude will experience a larger change in phase than those with a larger amplitude. Therefore, the regions that have low visibility amplitude also have very high phase variability as a direct consequence of the low amplitude (see also the discussion in Dexter et al. 2010).

Second, outside the confined locations of the amplitude minima, the variability in the visibility phases at small baseline lengths (less than a few  $G\lambda$ ) is, in general, very small, even though the accretion flow is highly turbulent. This happens because the small baselines primarily probe the overall structure of the image, which is determined by special and general relativistic effects rather than gas dynamics and shows little variability. However, at larger baseline lengths, for most baseline orientations, the SANE models A and B show

significant phase variability, while the MAD models C–E remain relatively quiet. The large baselines probe the small-scale structures, which, in the case of the SANE models, are dominated by, e.g., small hot magnetic flux tubes that are highly variable. In the case of the MAD models, even the small-scale structure is dominated by the emission at the funnel footpoints and, for the models we consider here, the closure phases along large baseline triangles are not significantly variable.

In order to demonstrate one of the above points in a different way, we show in Figure 5 the overall anticorrelation between the average visibility amplitude throughout the u-v plane and the corresponding dispersion in the visibility phase. Indeed, the largest phase dispersions occur when the visibility amplitude is very low, i.e., at least an order of magnitude smaller than its maximum. As this figure demonstrates, this anticorrelation is independent of the particular cause of variability or the specifics of the models explored.

## 4. Closure Phases

As we discussed in the previous sections, millimeter VLBI experiments cannot measure absolute phase since the atmosphere introduces an arbitrary phase that is variable on a  $\approx 10$  s timescale. Instead, the EHT measures closure phases, defined as the sum of the phases at the corners of a triangle in u-v space that corresponds to three telescopes on Earth. Measuring closure phases removes the effects of the atmosphere and instrumental noise from the phase measurements, but cannot recover all absolute phase information, because there are never enough closure triangles to solve for all absolute phases.

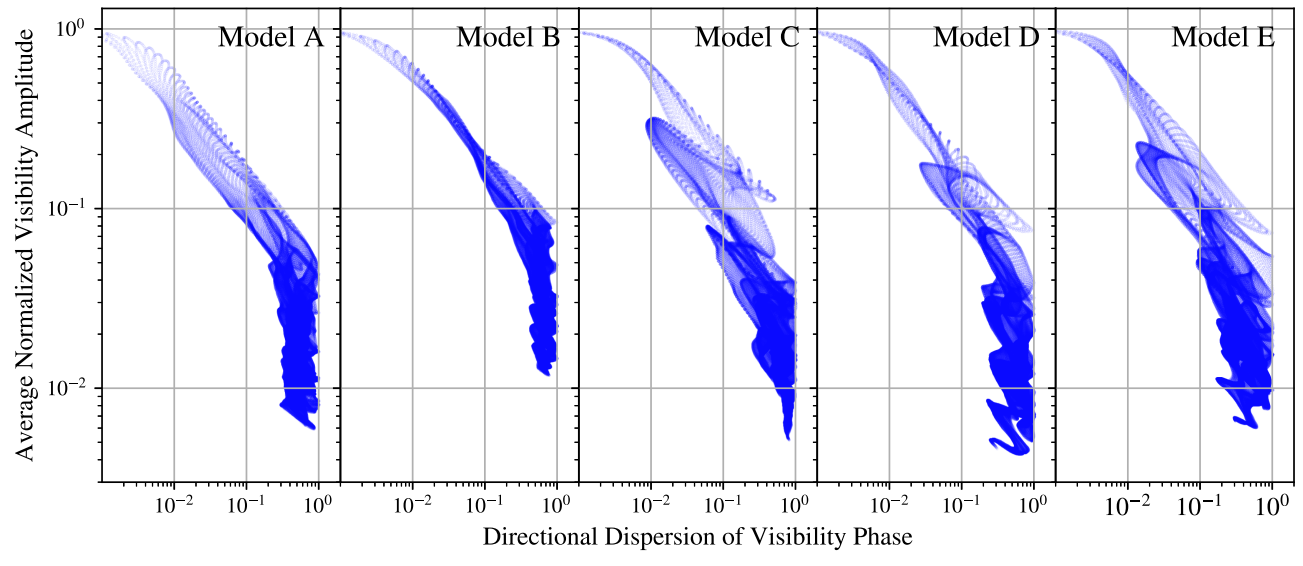


**Figure 5.** Normalized visibility amplitude vs. directional dispersion (D) of visibility phase. The different columns correspond to the different models and each dot is a point in u-v space. In all models, the regions of largest dispersion in visibility phase correspond to the lowest visibility amplitudes.

Our aim is to explore what the closure phases that the EHT measures will reveal about horizon-scale structures and how they will probe small-scale variability. During the span of an observation, closure triangles move through the u-v space. Therefore, the observed variability in closure phases will reflect the combined effect of the intrinsic variability of the source, the variability caused by the fact that the closure triangles are probing different parts of u-v space as the Earth rotates (see, e.g., Doeleman et al. 2009b; Broderick et al. 2011, 2016; Fraga-Encinas et al. 2016), and the variability caused by diffractive scattering effects (see Johnson & Gwinn 2015). In the current section, we are primarily interested in exploring the intrinsic variability caused by the accretion flow itself. Because of this, we keep the triangles constant in time for the majority of our analysis (fixed at GMST 01:54:03.4706); we will explore the effect of the Earth's rotation at the end of this section and the effects of scattering in a forthcoming paper.

We choose four representative triangles of varying shapes and sizes, shown in Figure 6. The smallest triangle, shown in red, is the Hawaii (Submillimeter Array-SMA)-Arizona (Submillimeter Telescope-SMT)-California (Combined Array for Research in Millimeter-wave Astronomy-CARMA) triangle. This is the only triangle on which the EHT has observed closure phases to date. The next smallest triangle, shown in magenta, is the Arizona (SMT)-Mexico (Large Millimeter Telescope-LMT)-Chile (Atacama Large Millimeter/submillimeter Array-ALMA) triangle. The bigger triangles are Arizona (SMT)-Chile (ALMA)-South Pole (South Pole Telescope-SPT), shown in green, and Hawaii (SMA)-Arizona (SMT)-South Pole (SPT), shown in blue.

We calculate closure phases for the four triangles for each snapshot of our five models, for black holes with spin axes pointing north and east. Due to the symmetry of Fourier transforms, the closure phases for black holes with spin axes pointing south (west) are the negative of the closure phase for black holes pointing north (east). We use the same sign convention as described in Fish et al. (2016). Figures 7 and 8 show closure phases as a function of time for both spin orientations, for the four triangles (ordered from the smaller triangle in the top row to the largest in the bottom row), and for

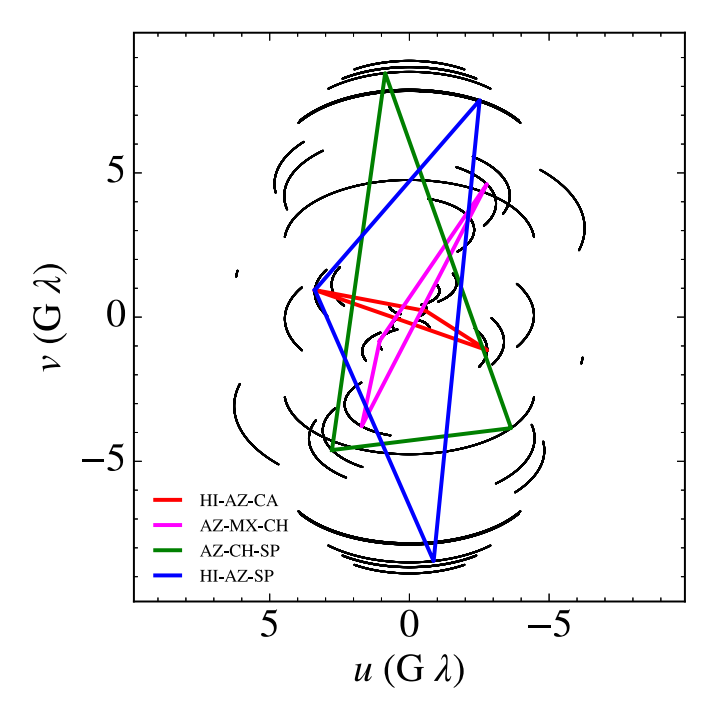


**Figure 6.** The four triangles we used to calculate closure phases (shown here at GMST 01:54:03.4706). In order of increasing size, they are Hawaii (SMA)-Arizona (SMT)-California (CARMA), shown in red, Arizona (SMT)-Mexico (LMT)-Chile (ALMA), shown in magenta, Arizona (SMT)-Chile (ALMA)-South Pole (SPT), shown in green, and Hawaii (SMA)-Arizona (SMT)-South Pole (SPT), shown in blue. The black curves correspond to the EHT baselines for reference. These triangles move through u-v space following the baseline tracks as the Earth rotates.

the five models. To explore the distribution of closure phases more quantitatively, we also plot them as histograms in Figure 9.

As the top panels for each model in Figures 7 and 8 and the leftmost panels in Figure 9 show, all of our GRMHD models produce little phase variability on small triangles, with the exception of situations where at least one vertex of the triangle crosses an amplitude minimum (see, e.g., the east orientation

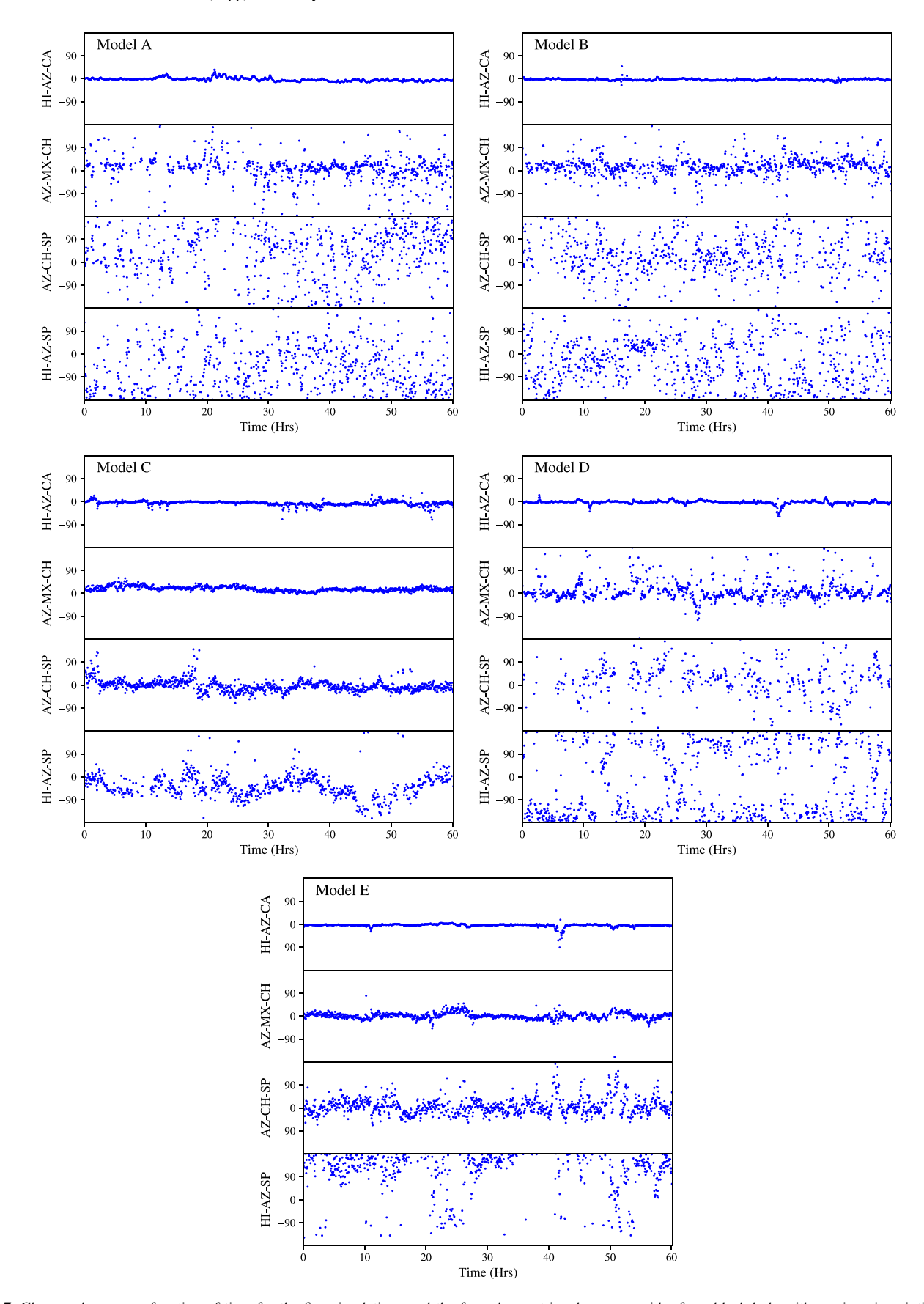


Figure 7. Closure phases as a function of time for the five simulations and the four closure triangles we consider for a black hole with a spin axis pointing north. Different rows correspond to different triangles in order of increasing size from top to bottom.

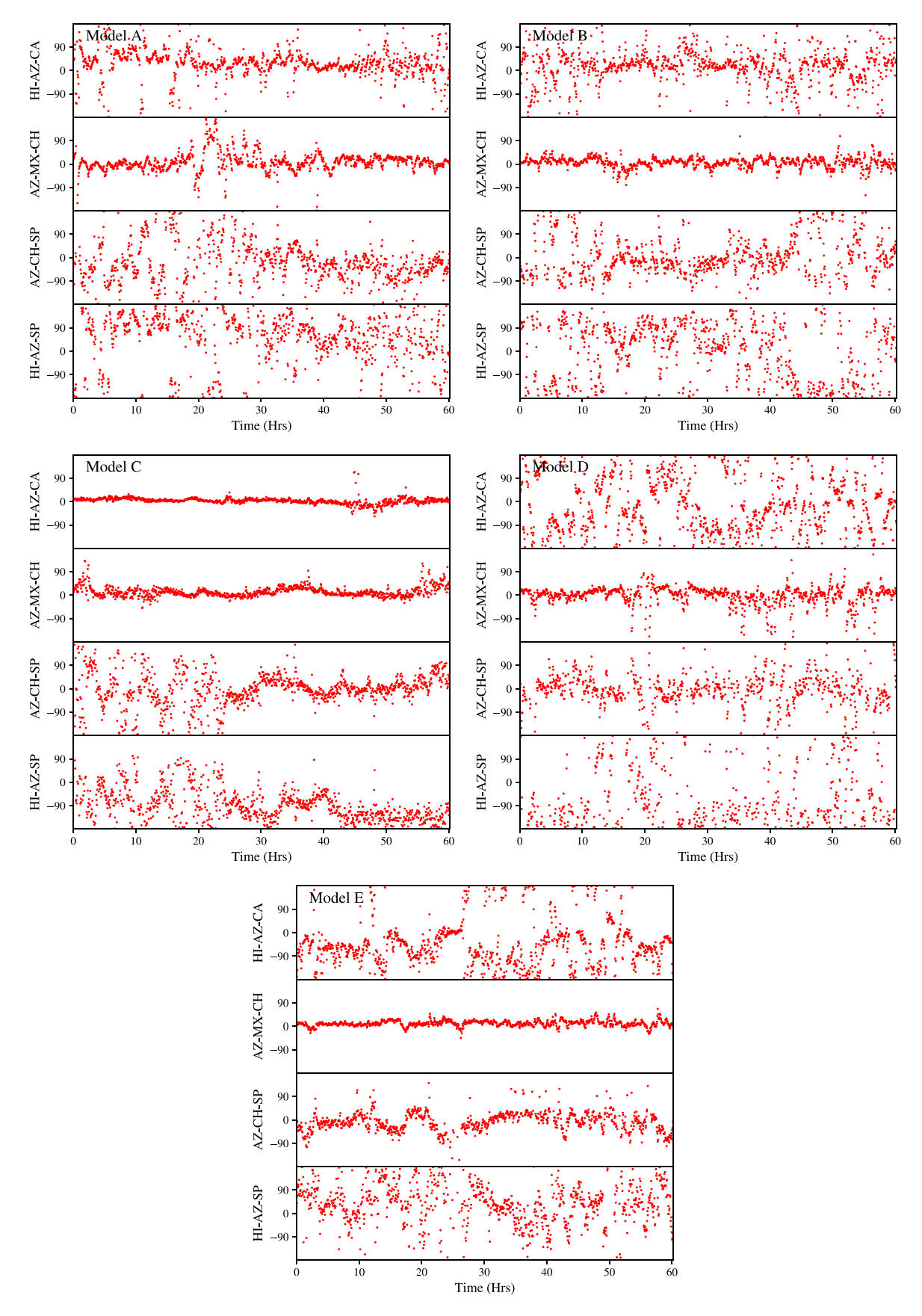


Figure 8. Same as Figure 7 but for a black hole with spin axis pointing east.

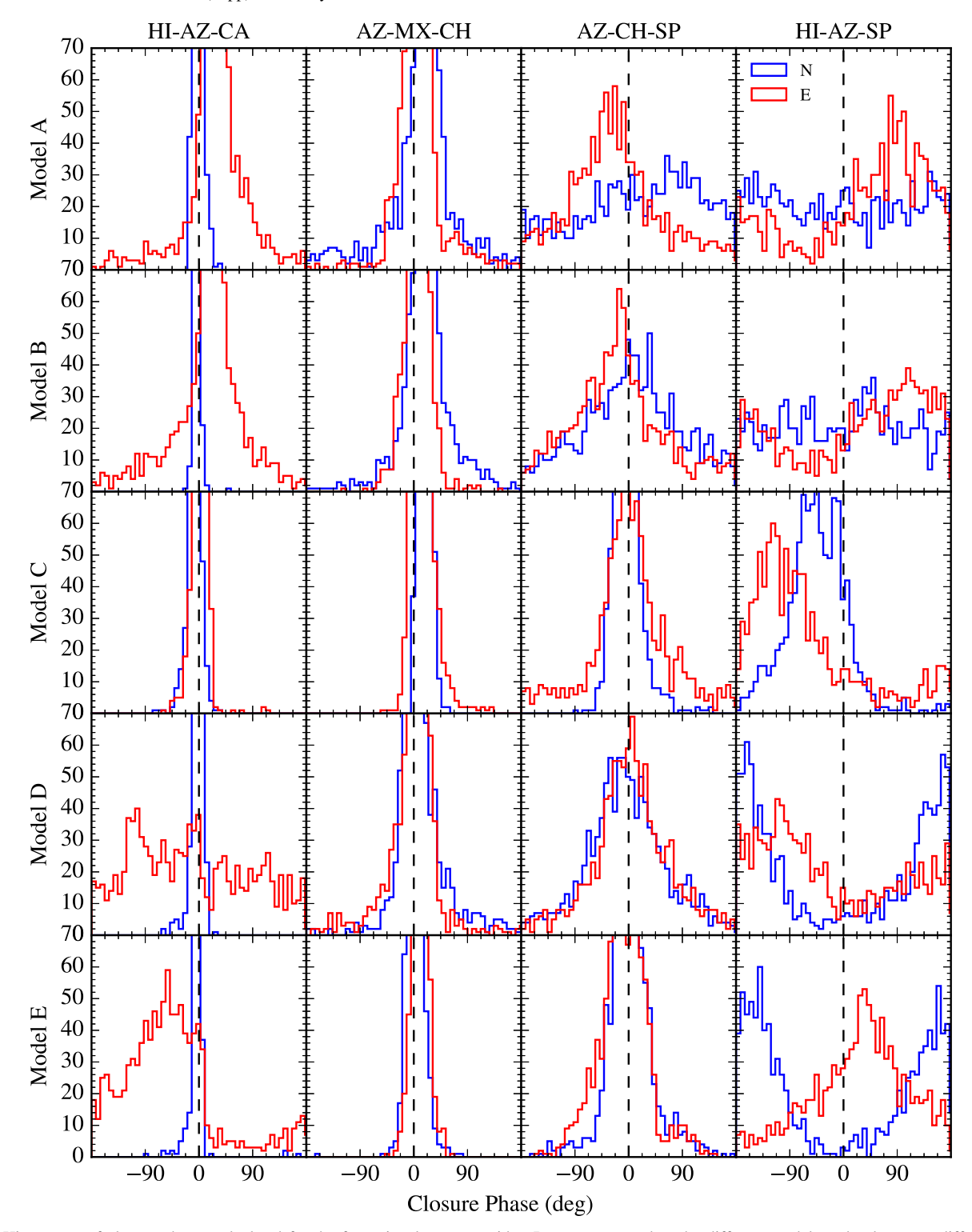
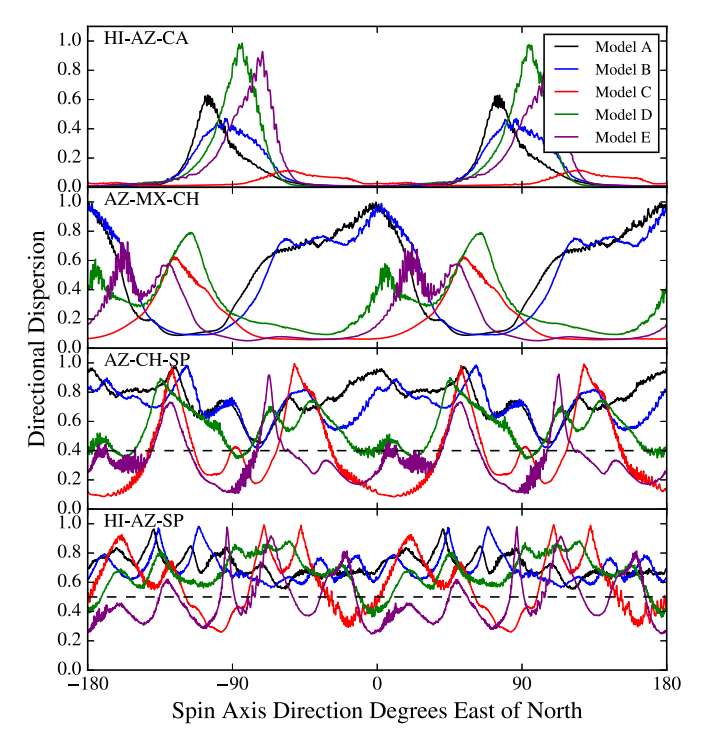


Figure 9. Histograms of closure phases calculated for the four triangles we consider. Rows correspond to the different models and columns to different closure triangles in order of increasing size. In all panels, the blue histograms correspond to a black hole with spin axis that points north, while the red histograms correspond to a spin axis that points east. The orientation of the black hole has a very large effect on the mean and width of the distribution of the closure phases. Some of the peaks of the histograms are not shown in this figure since we are not concerned primarily with the value of the peak but rather with the width of the distribution.

for models D and E). On larger triangles, the closure phases generally show larger dispersion. For these triangles, however, there is an important difference between the SANE and the MAD models. The MAD models still show peaked distributions of closure phases with well defined means and dispersions, whereas the histograms of the SANE models

become nearly flat. Both of these results are expected given our discussion of visibility phase variability in Section 3.

The results shown in Figures 7–9 are not specific to the particular black hole spin orientations chosen for these examples but are generically encountered in all orientations. We demonstrate this in Figure 10, which shows the dependence



**Figure 10.** Directional dispersion of closure phase for the four closure phase triangles we consider as a function of the orientation of the black hole spin axis. The black dashed line in the third panel corresponds to a directional dispersion of 0.4, which corresponds to a Gaussian with a dispersion of about 51°. The black dashed line in the fourth panel corresponds to a directional dispersion of 0.5, which corresponds to a Gaussian with a dispersion of about 57°.

of the closure phase dispersions on black hole orientation, for the four triangles and for the five models we consider here. In the smallest of the triangles, a small phase dispersion (at the level recently reported by Fish et al. 2016) occurs for about half of the spin-orientation parameter space for all five models. However, for the largest triangles, the large dispersion in the SANE models persists for all spin orientations.

The statistical properties of closure phase variability that we discussed so far correspond to fixed orientations of the baseline triangles on the u-v plane. In practice, we can observationally infer these properties if we combine data from different epochs and stack them based on the location of each triangle on the u-v plane. However, in the course of a single observation epoch, the orientation of each baseline triangle changes in time and the measured closure phases will sample different locations of the u-v plane, while the underlying image is varying at the same time. A consequence of this may be that a given triangle will rotate from a region of small variability to one of large variability (e.g., near a visibility minimum) or vice versa in the course of a night. In this case, the characteristics of phase variability will change dramatically in the course of the observation.

We show an example of this situation in Figure 11 for the small HI–AZ–CA triangle (top panels) and the SANE model A as well as for the larger AZ–MX–CH triangle (bottom panels) and for MAD model E, for two different orientations of the black hole spin. In two of the configurations shown (Model A, HI–AZ–CA south orientation and Model E AZ–MX–CH east orientation), the closure phase remains very stable throughout the observation, because the triangles remain away from the locations of the amplitude minima. In a third configuration (Model A, east orientation), the HI–AZ–CA triangle can follow

Sgr A\* for  $\simeq$ 4 hr. Because the size of this baseline track is comparable to the extent of the high-variability region, the closure phase is variable throughout the observation. In the last configuration (model E, north orientation), only a part of the longer ( $\simeq$ 6 hr) baseline track cuts through the region of high variability, causing a very sudden decline in the closure phase variability in the midst of the observation.

#### 5. Discussion and Conclusions

We used five GRMHD+radiative transfer simulations of accretion onto Sgr A\* to explore the predicted magnitudes of closure phases and their variability for the upcoming interferometric observations with the EHT. We now compare these predictions to existing data to asses the prospects of distinguishing between different models and black hole spin orientations. Currently, there exist only limited measurements of the closure phases, spanning different epochs, along the HI–AZ–CA triangle. These yield a median value of 6.3<sup>+0.7</sup><sub>-2.0</sub> degrees (Fish et al. 2016).

Statistically comparing the predicted distribution of closure phases to the observed ones requires separately treating the formal and systematic uncertainties in the measurements. Because the variability in Sgr A\*, as inferred both observationally (Meyer et al. 2008; Dexter et al. 2014) and from theoretical models (e.g., Dolence et al. 2012 and Chan et al. 2015a), points to a red noise process, comparing theoretical models to observations also requires incorporating the effects of finite observing time. We will perform a detailed comparison taking into account these considerations in a future study.

For a more preliminary comparison, we plot in Figure 12 not only the median measured closure phase but also a gray band that corresponds to the range of median values in the various subsets of the data in Fish et al. (2016). Even though both the disk-dominated SANE models and the funnel-dominated MAD models we analyzed here have significant asymmetric structures, Figure 12 shows that they produce closure phases and dispersions (Figure 10) in the HI–AZ–CA triangle that are consistent with the measurements for a wide range of black hole spin orientations on the sky.

In the near future, closure phases will be detected with the full EHT array over a wide range of baseline triangles, covering long tracks in the u–v plane. Our models show that, for triangles with sizes similar to that of the existing measurements, the closure phases will show little variability, unless one of the baseline vertices crosses a region of low visibility amplitude. However, the turbulent nature of the flow introduces significant variability on the small scales and, hence, significant closure phase variability might be present at large baseline triangles.

Despite this overall trend, the funnel-dominated MAD models that we studied produce less closure phase variability on the large triangles than the disk-dominated SANE models. This is because the images of the former are dominated by emission at the footpoints of the funnels and, even though these footpoints flicker, their image structure is not greatly influenced by the variability in the turbulent accretion flow. Therefore, future data will help distinguish between these possibilities. Furthermore, for both SANE and MAD models, we find that there is no trend between flaring events (see, e.g., Figure 1 in Medeiros et al. 2016) and higher closure phase variability.

Because the highest dispersion in phase occurs at low visibility amplitude, the question of detectability arises when

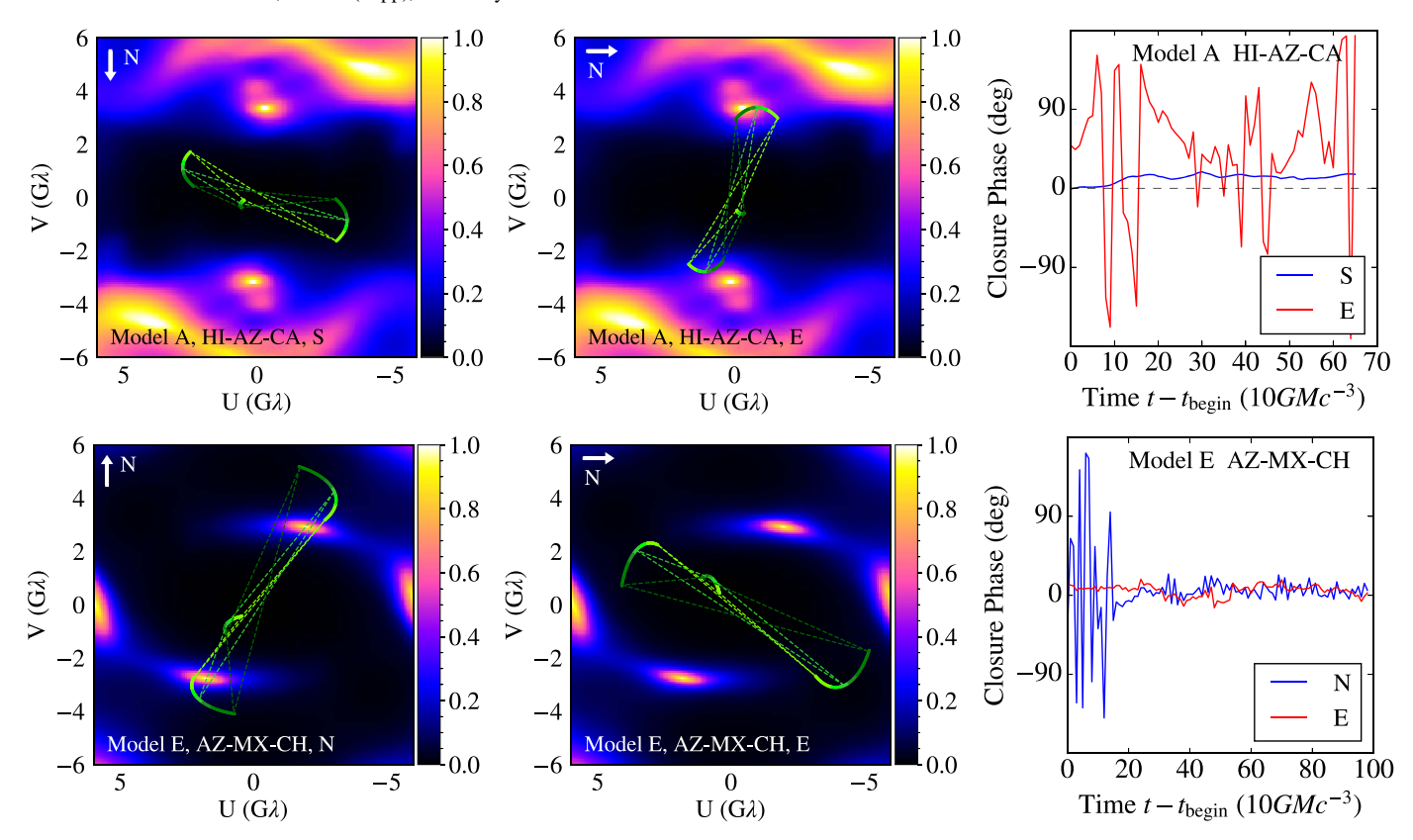
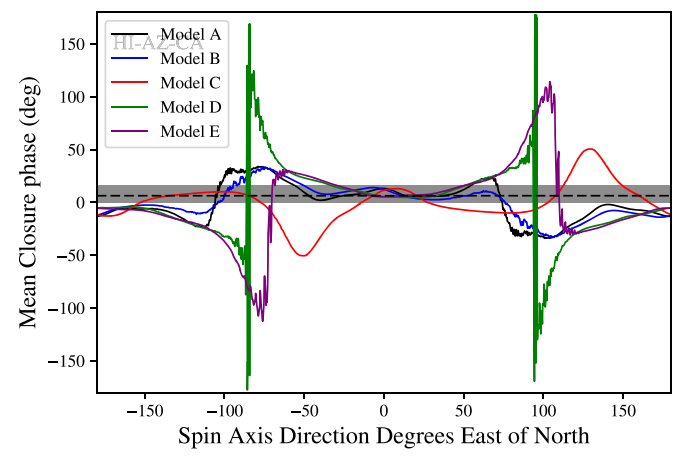


Figure 11. Effect of Earth rotation on the variability of closure phases. The top two color maps show the directional dispersion of Model A, the green tracks and dashed triangles correspond to the HI–AZ–CA closure triangle for a black hole pointing south (left panel) and east (middle panel). The bottom two color maps show the directional dispersion of Model E, the green tracks and dashed triangles correspond to the AZ–MX–CH closure triangle for a black hole pointing north (left panel) and east (middle panel). During the course of an observation, both closure triangles move from light green to dark green. The rightmost column shows how closure phase varies as a function of time due to the combined effect of intrinsic variability from the simulation and the motion of the closure triangles shown in the color maps. Depending on the orientation of the black hole, the rotation of the Earth may move the triangles to regions of high variability of closure phases during an observation.



**Figure 12.** Directional mean closure phase for the HI–AZ–CA triangle (in degrees) as a function of the orientation of the black hole spin axis. The dashed black line corresponds to the median closure phase measured by the EHT for this triangle (Fish et al. 2016). The gray band corresponds to the range of median values in the various subsets of the data in Table 3 of Fish et al. (2016).

discussing the potential of observing such large dispersions. The EHT has already detected fringes at levels below 10% of the flux at zero baseline (Johnson et al. 2015). Additionally, the incorporation of ALMA into the EHT array (2017 April) is expected to increase the sensitivity of the latter by at least a factor of a few. In most models, the directional dispersion (D) is of order unity in places in u-v space where the visibility

amplitude is 5% of the zero baseline flux (see Figure 5), indicating that regions with dispersion of order unity will be detectable if present. Even with improved sensitivity, we also expect regions and periods of low visibility amplitudes that fall below the signal-to-noise threshold. In such cases, following a non-detection, we expect that when the source is detected again, the phase will be uncorrelated with the prior phase due to the highly variable nature of phases near regions of minima in visibility amplitude.

Our results have important implications for the image reconstruction techniques that will rely on the closure phase data. Because of the possibility of substantial dispersion, even at small triangles, large amounts of high-quality data will need to be used to characterize the variability properties of the closure phases. Image reconstruction techniques will then need to take explicitly into account the observed variability. Alternatively, if image reconstruction techniques are used that rely on the assumption of a stationary image, the regions of high closure phase variability will need to be excised.

L.M. acknowledges support from NSF GRFP grant DGE 1144085. C.K.C., D.P., and F.O. were partially supported by NASA/NSF TCAN award NNX14AB48G and NSF grants Chandra Award No. TM6-17006X and AST 1312034. D.M. acknowledges support from NSF grant AST-1207752. F.O. gratefully acknowledges a fellowship from the John Simon Guggenheim Memorial Foundation in support of this work.

D.P. acknowledges support from the Radcliffe Institute for Advanced Study at Harvard University. All ray-tracing calculations were performed with the ElGato GPU cluster at the University of Arizona that is funded by NSF award 1228509.

## Appendix Directional Statistics

Calculating statistical moments of distributions of quantities that are periodic in nature, such as closure phases, requires special care. Mardia & Jupp (1999) explore meaningful ways of determining the mean and dispersion of distributions of angles. Specifically, they suggest that the mean of a distribution of n angles  $\theta_i$  may be obtained using

$$\bar{\theta} = \begin{cases} \tan^{-1}(\bar{S}/\bar{C}), & \text{if } \bar{C} \geqslant 0\\ \tan^{-1}(\bar{S}/\bar{C}) + \pi, & \text{if } \bar{C} < 0, \end{cases}$$
(1)

where

$$\bar{S} = \frac{1}{n} \sum_{i=1}^{n} \sin(\theta_i),\tag{2}$$

$$\bar{C} = \frac{1}{n} \sum_{j=1}^{n} \cos(\theta_j). \tag{3}$$

In other words, to calculate the mean of a distribution of angles, we calculate the mean of the unit vectors that correspond to the distribution of angles. The dispersion of a distribution of angles then is defined as

$$D = \frac{1}{n} \sum_{j=1}^{n} \{1 - \cos(\theta_j - \bar{\theta})\}. \tag{4}$$

Hereafter, we will refer to this dispersion relation as the directional dispersion when comparing it to the dispersion relation commonly used for non-directional data.

To understand the behavior of the directional dispersion, we consider here two limiting cases. For a small deviation from the mean  $(\theta_j - \bar{\theta})$ , the directional dispersion can be approximated as

$$D \simeq \frac{1}{n} \sum_{j=1}^{n} \left[ 1 - \left( 1 - \frac{(\theta_{j} - \bar{\theta})^{2}}{2} \right) \right]$$

$$= \frac{1}{2n} \sum_{j=1}^{n} \left[ (\theta_{j} - \bar{\theta})^{2} \right]$$

$$= \frac{\sigma^{2}}{2},$$
(5)

where we have denoted the normal definition of dispersion by  $\sigma$ .

In the limit of a continuous flat distribution of deviations from the mean, on the other hand, we find

$$D \simeq \frac{1}{2\pi} \int_{-\pi}^{\pi} \left[ 1 - \cos(\theta_j - \bar{\theta}) \right] d\theta$$
$$= 1 - \frac{1}{2\pi} \int_{-\pi}^{\pi} \cos(\theta_j - \bar{\theta}) d\theta$$
$$= 1. \tag{6}$$

In Figure 13, we explore the behavior of the directional dispersion further by comparing this quantity to the dispersion

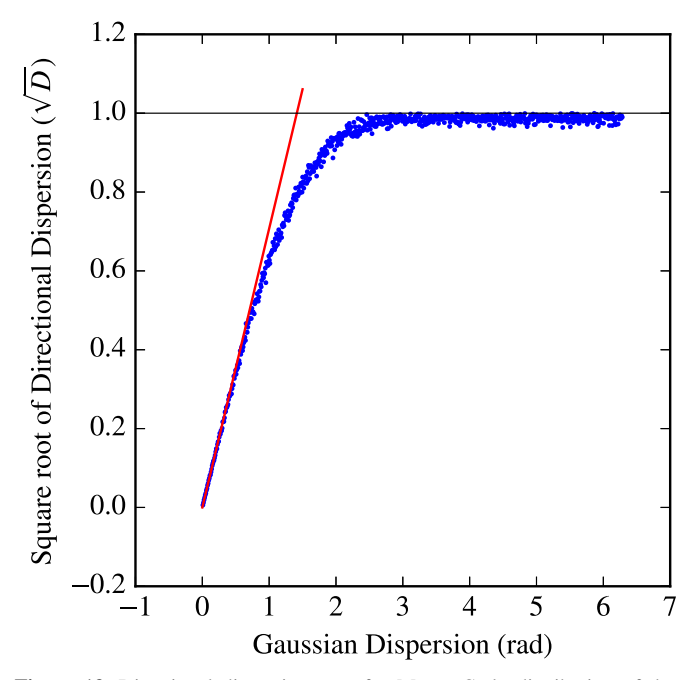


**Figure 13.** Directional dispersion, D, of a Monte Carlo distribution of data calculated using directional statistics as a function of the standard deviation of a Gaussian distribution that was used to create the Monte Carlo data. The red line corresponds to  $D = \sigma^2/2$ . The horizontal black line is at D = 1. As the standard deviation in the Monte Carlo simulation reaches  $\approx \pi$ , the directional dispersion approaches unity and remains constant as the standard deviation in the Monte Carlo increases further.

 $\sigma$  of an ensemble of Monte Carlo points drawn from a Gaussian distribution. The blue points are the square root of the directional dispersion of simulated data created using Gaussian distributions with different dispersions. As expected, the directional dispersion scales with the dispersion of the Gaussian distribution when the latter is small. However, as  $\sigma \gtrsim \pi$ , the periodic nature of the angular data causes the directional dispersion to asymptote to unity.

## References

Baganoff, F. K., Bautz, M. W., Brandt, W. N., et al. 2001, Natur, 413, 45

Ball, D., Özel, F., Psaltis, D., & Chan, C.-K. 2016, ApJ, 826, 77 Broderick, A. E., Fish, V. L., Doeleman, S. S., & Loeb, A. 2011, ApJ, 738, 38 Broderick, A. E., Fish, V. L., Johnson, M. D., et al. 2016, ApJ, 820, 137 Chan, C.-K., Psaltis, D., & Özel, F. 2013, ApJ, 777, 13 Chan, C.-K., Psaltis, D., Özel, F., et al. 2015a, ApJ, 812, 103 Chan, C.-K., Psaltis, D., Özel, F., Narayan, R., & Sadowski, A. 2015b, ApJ, 799, 1 Dexter, J., Agol, E., Fragile, P. C., & McKinney, J. C. 2010, ApJ, 717, 1092 Dexter, J., Kelly, B., Bower, G. C., et al. 2014, MNRAS, 442, 2797 Do, T., Ghez, A. M., Morris, M. R., et al. 2009, ApJ, 691, 1021 Doeleman, S., Agol, E., Backer, D., et al. 2009a, Ast, 2010, 68 Doeleman, S. S., Fish, V. L., Broderick, A. E., Loeb, A., & Rogers, A. E. E. 2009b, ApJ, 695, 59 Doeleman, S. S., Phillips, R. B., Rogers, A. E. E., et al. 2002, in Proc. 6th EVN Symp., New Developments in VLBI Science and Technology, ed. E. Ros et al. (Bonn: Max-Planck-Institut für Radioastronomie), 223 Doeleman, S. S., Weintroub, J., Rogers, A. E. E., et al. 2008, Natur, 455, 78 Dolence, J. C., Gammie, C. F., Shiokawa, H., & Noble, S. C. 2012, ApJL, Fish, V. L., Doeleman, S. S., Beaudoin, C., et al. 2011, ApJL, 727, L36 Fish, V. L., Johnson, M. D., Doeleman, S. S., et al. 2016, ApJ, 820, 90 Fraga-Encinas, R., Mościbrodzka, M., Brinkerink, C., & Falcke, H. 2016, &A, 588, A57 Gammie, C. F., McKinney, J. C., & Tóth, G. 2003, ApJ, 589, 444 Genzel, R., Schödel, R., Ott, T., et al. 2003, Natur, 425, 934 Ghez, A. M., Salim, S., Weinberg, N. N., et al. 2008, ApJ, 689, 1044 Gillessen, S., Eisenhauer, F., Trippe, S., et al. 2009, ApJ, 692, 1075

Howes, G. 2011, ApJ, 738, 40
Howes, G. G. 2010, MNRAS, 409, L104
Jennison, R. C. 1958, MNRAS, 118, 276
Johannsen, T., Psaltis, D., Gillessen, S., et al. 2012, ApJ, 758, 30
Johnson, M. D., Fish, V. L., Doeleman, S. S., et al. 2015, Sci, 350, 1242
Johnson, M. D., & Gwinn, C. R. 2015, ApJ, 805, 180
Lu, R.-S., Roelofs, F., Fish, V. L., et al. 2016, ApJ, 817, 173
Mardia, K., & Jupp, P. 1999, Directional Statistics (1st ed.; Chichester: Wiley)
Marrone, D. P., Baganoff, F. K., Morris, M. R., et al. 2008, ApJ, 682, 373

Medeiros, L., Chan, C.-K., Ozel, F., et al. 2016, arXiv:1601.06799
Meyer, L., Do, T., Ghez, A., et al. 2008, ApJL, 688, L17
Narayan, R., Sądowski, A., Penna, R. F., & Kulkarni, A. K. 2012, MNRAS, 426, 3241
Neilsen, J., Nowak, M. A., Gammie, C., et al. 2013, ApJ, 774, 42
Porquet, D., Grosso, N., Predehl, P., et al. 2008, A&A, 488, 549
Ressler, S. M., Tchekhovskoy, A., Quataert, E., & Gammie, C. F. 2017, MNRAS, 467, 3604
Sądowski, A., Narayan, R., Penna, R., & Zhu, Y. 2013, MNRAS, 436, 3856